Asymetrical shape of C–He lines in the ultraviolet

Nicole F. Allard, Fernand Spiegelman

▶ **To cite this version:**

Nicole F. Allard, Fernand Spiegelman. Asymetrical shape of C–He lines in the ultraviolet. Monthly Notices of the Royal Astronomical Society, 2024, 529 (3), pp.2527-2538. 10.1093/mnras/stae477 . hal-04564285

HAL Id: hal-04564285
https://hal.science/hal-04564285

Submitted on 5 May 2024

HAL is a multi-disciplinary open access archive for the deposit and dissemination of scientific research documents, whether they are published or not. The documents may come from teaching and research institutions in France or abroad, or from public or private research centers.

L'archive ouverte pluridisciplinaire **HAL**, est destinée au dépôt et à la diffusion de documents scientifiques de niveau recherche, publiés ou non, émanant des établissements d'enseignement et de recherche français ou étrangers, des laboratoires publics ou privés.

Distributed under a Creative Commons Attribution 4.0 International License

Monthly Notices of the ROYAL ASTRONOMICAL SOCIETY

MNRAS **529,** 2527–2538 (2024) https://doi.org/10.1093/mnras/stae477
Advance Access publication 2024 March 15

Asymetrical shape of C–He lines in the ultraviolet

Nicole F. Allard [1,2]★ and Fernand Spiegelman[3]★

[1]*GEPI, Observatoire de Paris, Université PSL, UMR 8111, CNRS, 61, Avenue de l'Observatoire, F-75014 Paris, France*
[2]*Institut d'Astrophysique de Paris, Sorbonne Université, CNRS, UMR 7095, 98bis Boulevard Arago, F-75014 Paris, France*
[3]*Laboratoire de Physique et Chimie Quantique, Fédération FERMI, Université de Toulouse (UPS) and CNRS, 118 route de Narbonne, F-31400 Toulouse, France*

Accepted 2024 February 12. Received 2024 February 8; in original form 2023 December 3

ABSTRACT

We present the first theoretical line profile calculations of the ultraviolet spectral lines of carbon perturbed by helium using a semiclassical collision approach and high-quality *ab initio* potentials and electronic transition dipole moments. The temperature range is from 5000 to 8000 K. These results are important for astrophysical modelling of spectra in atmospheres of white dwarf stars showing atomic carbon in an helium atmosphere. Beyond the conventional symmetrical Lorentzian core at low He density, these lines exhibit a blue asymmetric behaviour. This blue asymmetry is a consequence of low maxima in the corresponding C–He potential energy difference curves at short internuclear distances. The collisional profiles are carefully examined and their perturber density dependence allow to understand the various line shapes of the observed carbon spectral lines in helium-rich white dwarf photosphere where the He perturber densities reach several 10^{21} cm^{-3}.

Key words: line: formation – line: profiles – stars: atmospheres – white dwarfs.

1 INTRODUCTION

The theory of stellar evolution predicts that the majority of white dwarfs have a core made of carbon and oxygen, which itself is surrounded by a helium layer. White dwarf stars of spectral type DQ are defined as showing atomic or molecular features of carbon in an helium atmosphere, they are of special interest, because they provide information about the deeper layers of the stars. The presence of carbon is believed due to a process of convective dredge-up of C which mixes into the outer He layers (Koester, Weidemann & Zeidler 1982; Pelletier et al. 1986). For white dwarfs with available spectroscopic observations in the ultraviolet (UV) strong asymmetric absorption features have been observed. Fig. 1 shows the *International Ultraviolet Explorer* (*IUE*) observation of L97-3, its spectrum contains the C lines at 1657, 1930, and 2478 Å studied in this paper. White dwarf spectra shown in the paper are extracted from Holberg, Barstow & Burleigh (2003). The Space Telescope Imaging Spectrograph was also used by Provencal et al. (2002) to obtain the spectrum of Procyon B. Its *Hubble Space Telescope* (*HST*) spectrum in the UV shown in Fig. 1 contains the asymmetric C lines at 1930 and 2478 Å. Fig. 1 clearly shows also the Mg^+ resonance lines near 2800 Å, Procyon B is then classified as a DQZ white dwarf, with an effective temperature $\sim$ 7 740 K (Provencal et al. 2002) near the value previously determined from *HST* photometry $\sim$ 8000 K (Provencal et al. 1997).

The current synthetic spectra do not account for the asymmetrical shape of these carbon lines. The van der Waals broadening treatment within the impact approximation, widely used in model atmospheres, is inadequate to the task. The only physical approach was done in Koester et al. (1982) using the unified Franck–Condon theory of Szudy & Baylis (1975) with a Lennard-Jones (6-12) potential for the interaction. The fit to the observation was better but convinced the authors that more accurate potentials were required. Moreover, cool, helium-rich white dwarfs are characterized by high photospheric densities, in these physical conditions no accurate opacities of the atomic carbon lines included in the current atmosphere models exist. The broad singlet line at 1930 Å shown in the bottom of Fig. 1 could not be reproduced by Weidemann & Koester (1995) using van der Waals broadening. The model shortcomings are a consequence of the high-density environments in cool helium-rich white dwarf photosphere. Helium densities, $n_{\rm He} = 1 \times 10^{21}$ cm^{-3} and above require the use of a general unified theory valid at high perturber densities. This challenge has motivated us to study the C–He collisional profiles for the physical conditions prevailing in the atmosphere of cool DQ white dwarfs where these lines are observed. Neutral collision broadening depends on the knowledge of neutral atom interactions and it is only relatively recently that the *ab initio* methodology for computing energies of atom pairs has developed the extreme precision needed to provide these data by several authors (Lavendy, Robbe &. Roueff 1991; Staemmler & Flower 1991; Partridge, Stallcop & Levin 2001; Le Picard et al. 2002; Bergeat et al. 2018), no electronic structure data were available for the higher states. Significant progress in the description of C–He singlet and triplet excited states has been achieved by Cargnoni (2023) through multireference configuration interaction (MRCI) calculations. The purpose of this work is to make an exhaustive study of the singlet C lines at 1930 and 2478 Å [transitions ^{1}D($2s^2 2p^2$) – ^{1}P($2s^2 2p 3s$) and

★ E-mail: nicole.allard@obspm.fr (NFA); spiegelman@irsamc.ups-tlse.fr (FS)

© 2024 The Author(s).
Published by Oxford University Press on behalf of Royal Astronomical Society. This is an Open Access article distributed under the terms of the Creative Commons Attribution License (http://creativecommons.org/licenses/by/4.0/), which permits unrestricted reuse, distribution, and reproduction in any medium, provided the original work is properly cited.

Downloaded from https://academic.oup.com/mnras/article/529/3/2527/7630239 by guest on 05 May 2024

$^1S(2s^22p^2)$ – $^1P(2s^22p3s)$, respectively] and of the resonance triplet line at 1657 Å [transition $^3D(2s^22p^2)$ - $^3P^o(2s^22p3s)$].

This paper is in continuation with our analysis of the Mg^+ line observed in Procyon B. For that purpose, intensive *ab initio* calculations were performed to obtain the ground and first excited potential energy curves (PECs) for the Mg^+–He system (Allard et al. 2016b). Procyon B, the third brightest white dwarf known, is a critical object for testing the fundamental physics of stellar degeneracy.

We have redetermined the PECs and transition dipole moments of CHe using an MRCI (Werner & Knowles 1988) scheme similar to that used by Cargnoni (2023), however conducted with larger basis sets and more extensive CI spaces, and also exploring the behaviour at shorter internuclear distances. We report in Section 2 the details of the calculations, the results, and comparison in particular with the data of Cargnoni (2023).

The unified line shape theory of Allard et al. (1999) and the set of atomic interaction potential energies described in Section 2 are used to model the entire line profile from the impact-broadened line centre to the far wing. This study takes place in a dipole autocorrelation formulation of the atomic line shape in a classical path trajectory approximation. After a rapid account of the unified theory of Allard et al. (1999) in Section 3 we report a theoretical analysis of the C–He line profiles in the physical conditions of atmospheres in cool DQ white dwarfs in Section 4.

2 C–HE POTENTIAL ENERGY CURVES AND ELECTRONIC TRANSITION DIPOLE MOMENTS

We have determined all the states for He interacting with $C(^3P, ^3P^o, ^3D^o)$ and with $C(^1D, ^1S, ^1P^o)$. The calculation for the ground and excited states energies was achieved via the MRCI scheme of the MOLPRO package (Werner & Knowles 1988; Werner et al. 2020). Atomic Gaussian type orbitals (GTO) basis sets with aug-cc-pv6z *spdfgh* quality were used on both carbon and hydrogen atoms, complemented by diffuse *s* and *p* functions on carbon with respective exponents 0.015 and 0.010 to ensure a satisfactory description of non-valence 3s and 3p orbitals. This resulted in a total basis of 319 GTOs significantly larger than that used in the work of Cargnoni (2023), namely cc-aug-pVTZ basis sets complemented by mid-bond functions. The above basis provide ground state static dipole polarizabilities of 1.383 a_0^3 and 11.638 a_0^3 for He and C atoms, respectively, to be compared with the recommended values given in Schwerdtfeger tables (Schwerdtfeger & Nagle 2019), 1.380 a_0^3 and 11.306 a_0^3, respectively. This should ensure a fair description of long range forces. The molecular calculations were made within the C_{2v} space point group available in MOLPRO as a subgroup of the proper $C_{\infty v}$ point group of the CHe molecule. The molecular orbitals were taken from Restricted Open Shell Hartree–Fock calculations of the $^2\Sigma^+$ state of the CHe^+ ion, providing equivalent π_x and π_y orbitals and expectedly better virtual orbitals than those of neutral CHe. The MRCI was generated from a reference complete active space (CAS) with 7/3/3/1 active orbitals in A_1, B_1, B_2, and A_2 symmetries respectively, yielding MRCI spaces with sizes of a few 10^8 contracted configurations, depending on the symmetries. The inner 1σ orbital (symmetry A_1) correlated with the 1s orbital of carbon remaining inactive. In the singlet case, the targeted numbers of roots in each symmetry manifold A_1, B_2, and A_2 of the C_{2v} point group were 4, 2, and 2, respectively, corresponding to determination of states $1^1\Sigma^+(^1D), 2^1\Sigma^+(^1S), 3^1\Sigma^+(^1P^o), 1^1\Pi(^1D), 2^1\Pi(^1P^o)$, and $1^1\Delta(^1D)$. Note that one component of the Δ states belongs to symmetry A_1,

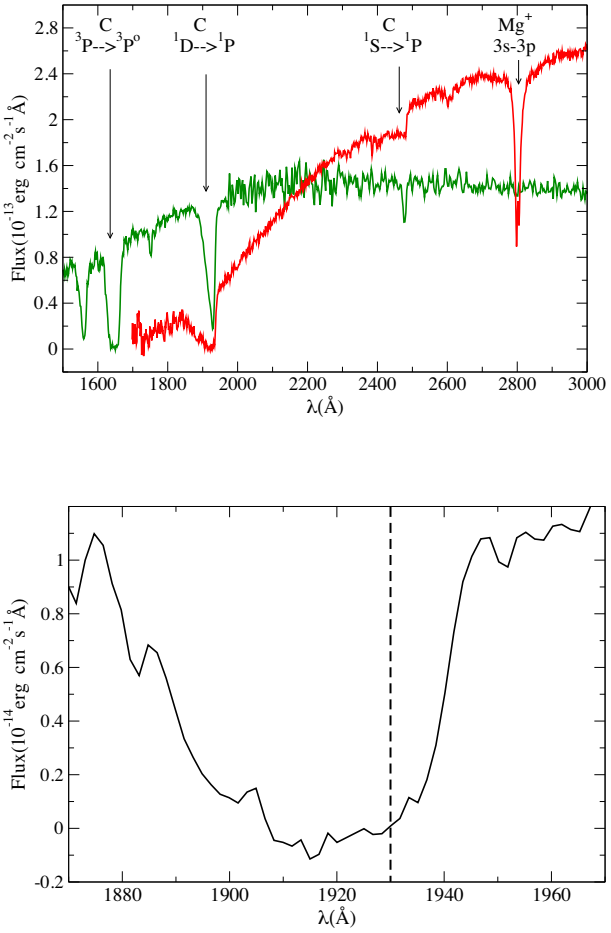

Figure 1. Top: *IUE* spectrum of LDS687A (Oswalt et al. 1991, green line) compared to *HST* spectrum of Procyon (Provencal et al. 2002, red line). Bottom: *IUE* spectrum of L845-70 (Weidemann & Koester 1995). The black dashed line gives the position of the unperturbed line.

while the second one belongs to symmetry A_2, which is accounted for in the desired roots. In the triplet case, the targeted number of roots was 2, 3, and 2 providing the description of states $1^3\Sigma^+$ ($^3P^o$), $1^3\Pi$ (^3P), $2^3\Pi$ ($^3P^o$), $3^3\Pi$ ($^3D^o$), $1^3\Sigma^-$ (^3P), and $1^3\Delta$ ($^3D^o$). CI convergence problems have occasionally been met due to intruder states. They were solved either by increasing the space initiating the CI resolution, or increasing the number of required roots.

We first discuss the triplet states potentials shown in Fig. 2. In the medium- and long-range parts, the states maintain their atomic character and have weak or very weak bonding, as found by Cargnoni (2023) and previous authors (Partridge et al. 2001; Le Picard et al. 2002; Bergeat et al. 2018). We therefore have not plotted again the detailed potential energies in the range $R \geq 7$ bohr in which these potentials have simple Van der Waals-like forms since the states correlated with the various asymptotes are decoupled from one another and are governed by the balance between the repulsive contribution and the dispersion forces. In Table 2, we list their medium- and long-distance bonding characteristics, in comparison with previous calculations available in the literature. The agreement is generally satisfactory, with the noticeable exception of the dissociation energy $D_e = 16\ cm^{-1}$ of state $1^3\Pi$ which we find significantly larger than that given by previous authors. One reason could be the use of a large basis set in this work. However the cause of discrepancy could paradoxically be the generation of the MRCI scheme by a rather

Downloaded from https://academic.oup.com/mnras/article/529/3/2527/7630239 by guest on 05 May 2024

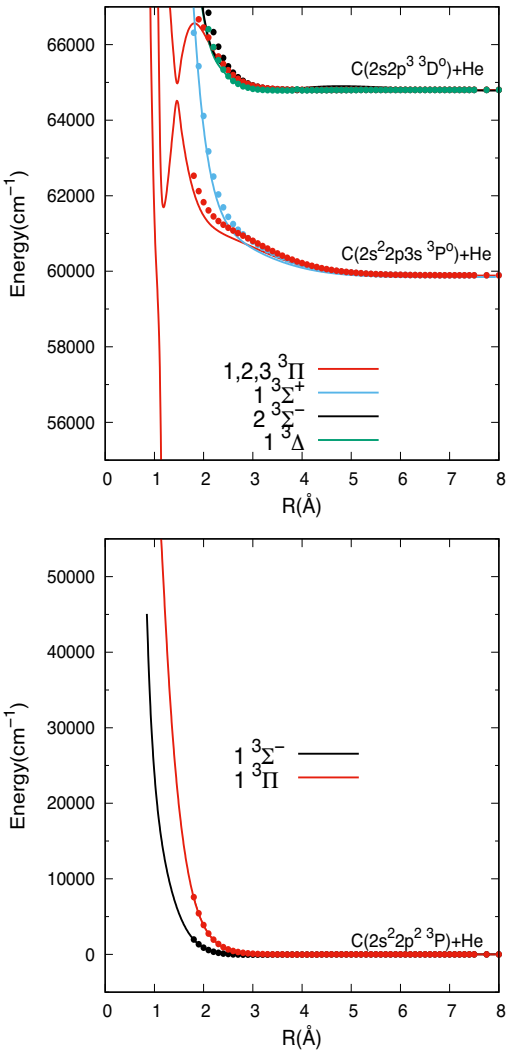

Figure 2. MRCI adiabatic PECs of triplet molecular states of C + He up to 67 000 cm^{-1} above the dissociated ground state energy. Bottom: states dissociating into C(^{3}D) + He; and top: states dissociating into C($^3P^o$, $^3D^o$) + He. The states numbering follows increasing energy within each symmetry manifold. The dotted potentials are the data of Cargnoni (2023).

Table 1. MRCI (this work) electronic transition energies of Carbon levels (in cm^{-1}). The calculated transition values are determined by averaging degenerate molecular states energies obtained at R = 50 bohr in different symmetries (the rms dispersion is less than 40 cm^{-1}, whatever the transition). Non-relativistic experimental transitions are $(2j + 1)$-weight averaged over the j spin–orbit terms, taken from NIST tables (Kramida et al. 2022).

Level	MRCI	Experimental
^{3}P ($2s^22p^2$)	0	0
^{1}D ($2s^22p^2$)	10361	10162
^{1}S ($2s^22p^2$)	21598	21618
$^1P^o$ ($2s^22p3s$)	61 818	61952
$^3P^o$ ($2s^22p3s$)	59 869	60373
$^3D^0$ ($2s2p^3$)	64 926	64059

Table 2. Comparison of the present medium- and long-distance equilibrium properties of the lowest CHe electronic states with literature data. State labelling (letters) used elsewhere (Cargnoni 2023) are given between parenthesis in the first column.

State	correlation	R_e(Å)	D_e(cm^{-1})	reference
$1^3\Sigma^-$ (X)	^{3}P	3.02	31.93	*a*
		3.02	32.46	*b*
		3.12	23.5	*c*
		2.99	34.28	*d*
		2.96	34.58	*e*
$1^3\Pi$ [A)	^{3}P	3.90	16.48	*a*
		3.91	9.26	*b*
		4.02	5.80	*c*
		3.86	8.98	*d*
		3.86	9.12	*e*
$2^3\Pi$ (B)	$^3P^o$	7.58	0.15	*a*
		8.29	0.37	*b*
$1^3\Sigma^+$ (C)	$^3P^o$	7.15	0.59	*a*
		8.33	0.36	*b*
$1^3\Delta$ (D)	$^3D^o$	3.78	10.62	*a*
		3.60	15.01	*b*
$2^3\Sigma^-$ (E)	$^3D^o$	–	–	*a*
		4.19	6.34	*b*
$3^3\Pi$ (F)	$^3D^o$	3.83	26.08	*a*
$1^1\Delta$ (a)	^{1}D	2.87	47.66	*a*
		2.81	52.23	*b*
$1^1\Sigma^+$ (b)	^{1}D	4.20	10.12	*a*
		3.99	13.83	*b*
$1^1\Pi$ (c)	^{1}D	4.15	11.67	*a*
		3.94	12.80	*b*
$2^1\Sigma^+$ (d)	^{1}S	4.25	6.74	*a*
		3.90	13.50	*b*
$2^1\Pi$ (e)	$^1P^o$	7.83	2.52	*a*
		8.71	0.33	*b*
$3^1\Sigma^+$ (f)	$^1P^o$	–	–	*a*
		8.53	0.15	*b*

Notes. Literature references are: *a*, MRCI this work; *b*, MRCI (Cargnoni 2023); *c*, CASPT2 (Le Picard et al. 2002); *d*, CCSD(T)(Partridge et al. 2001); and *e*, CCSD(T)(Bergeat et al. 2018).

large CAS space with non-valence orbitals, which does not ensure the stability of the its orbital content due to intruder states. Moreover, as compared with Coupled Cluster calculations involving simple and double plus perturbative triple excitations (CCSD(T)) which exist for the two lowest states (Partridge et al. 2001; Bergeat et al. 2018), MRCI is not size-consistent. At distances below 3 Å, all the states are characterized by a repulsive behaviour, the steeper ones being $1^3\Pi$ and $1^3\Sigma^+$ fully repulsive in the displayed range. However at even smaller distances (R < 2 Å), the electronic structure becomes more complex. Indeed, around R =1.2 Å, the repulsive potential wall of state$1^3\Pi$ undergoes an avoided crossing with state $2^3\Pi$, adiabatically correlated with asymptote $^3P^o$. The latter state $2^3\Pi$ is itself affected at R =1.8 Å by a weakly avoided crossing with state $3^3\Pi$ related to asymptote $^3D^o$. This results in a metastable minimum at R = 1.19 Å in state $2^2\Pi$ located 1810 cm^{-1} above its adiabatic dissociation limit with a barrier of 4552 cm^{-1}. It can be noted from Fig. 2 and Table 1 that in the region investigated by Cargnoni (R > 1.8 Å), the present potentials are consistent with his results, taken from its supporting information data (Cargnoni 2023).

The potential curves of the singlet states of CHe are shown in Fig. 3 all have repulsive walls at short distance. One can notice nevertheless that the highest states $2^1\Pi$ correlated with ^{1}P is characterized by inflexions in the repulsive walls between 1.5 and 3 Å, likely linked

Downloaded from https://academic.oup.com/mnras/article/529/3/2527/7630239 by guest on 05 May 2024

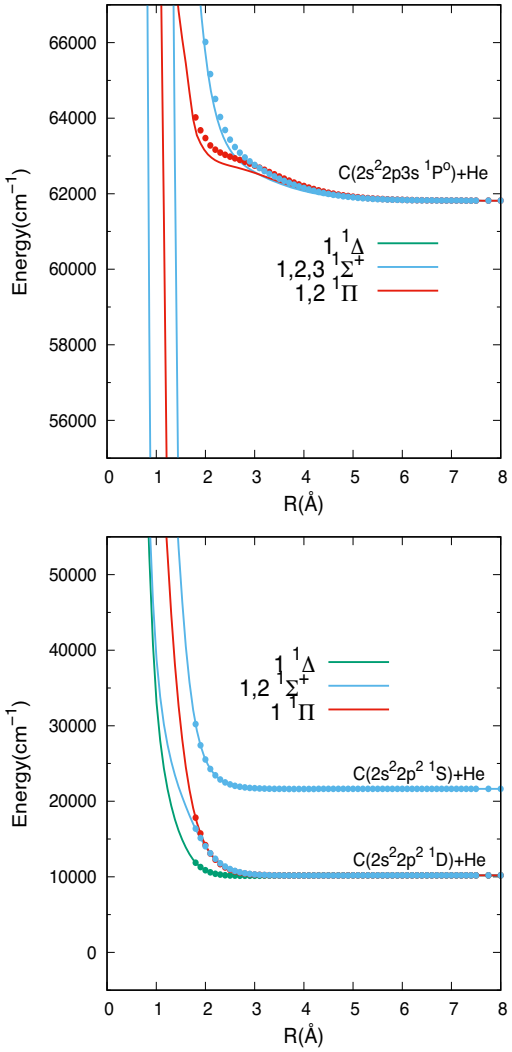

Figure 3. MRCI adiabatic PECs of singlet molecular states of C + He up to 67 000 cm^{-1} above the dissociated ground state energy. Bottom: states dissociating into C(^{1}) + He; and top: states dissociating into C(^{1}S,^{1}P) + He. The states numbering follows increasing energy within each symmetry manifold. The dotted potentials are the data of Cargnoni (2023).

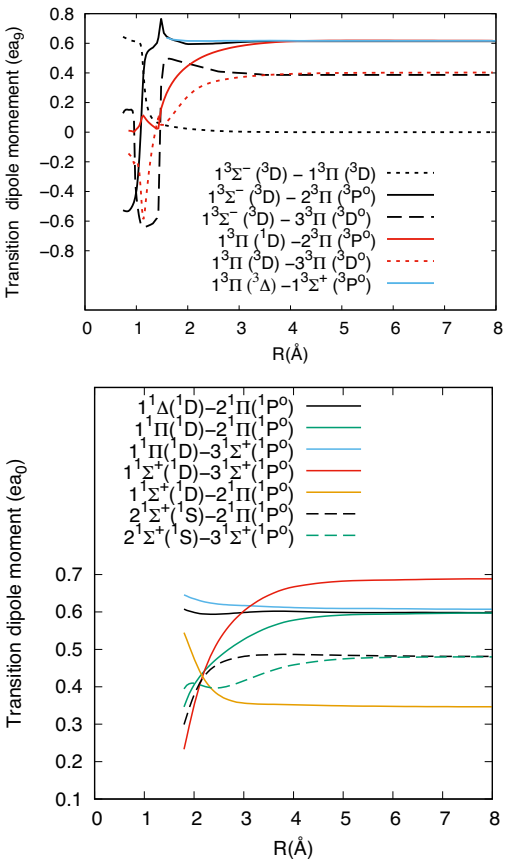

Figure 4. Transition dipole moments between adiabatic states of CHe. Bottom: transitions between singlet states; and top: transitions between triplet states; labelling of the states as in Figs 2 and 3.

to electronic configuration mixing, slightly more marked in our result than in the Cargnoni's potential. All singlet potentials are essentially repulsive, however all states are weakly bound except $2^1\Sigma^+(^1S)$ found purely repulsive. The most stable one is $^1\Delta(^1D)$ with a dissociation energy of 49 cm^{-1} at distance R_e = 3 Å. The results for singlet states are in line with the calculations of Cargnoni (2023) as can be seen in Fig. 3.

The transition moments within the triplet and singlet manifolds were calculated from the MRCI wavefunctions. They are are shown in Fig. 4. Three transitions from the molecular states originating from ^{3}D to those correlated with ^{3}P are allowed, all close to 0.6 a_0^3. The three asymptotic values are almost identical (around 0.6 a_0^3) as shown in Appendix A for the single configuration case. This provides a total transition line strength factor (sum of squares of the dipole moments d^2 of the degenerate transitions) of 6.30 a_0^6, to be compared with the value 6.045 a_0^6 summing the fine structure ^{3}D–^{3}P transition strengths taken from the US National Institute od Standards and Technology (NIST) spectral data tables (Haris & Kramida 2017). The triplet–triplet transition moments are relatively constant as functions of the internuclear distance and remain close to their asymptotic values down to R =4 Å. Below R = 2 Å, the transitions moments from the ground state $1^3\Sigma^-$ to the three Π states show strong and rapid variations. Since the ground state keeps a stable content, this is essentially caused by the successive avoided intercrossings of the $^3\Pi$ states around R =1.8 Å (barrier of state $3^3\Pi$ interacting with a higher state) and around R =1.2 Å (avoided crossing between states $2^3\Pi$ and $3^3\Pi$). The transition moments between triplet states $1^3\Pi - 2^3\Pi$ and $1^3\Pi - 3^3\Pi$ both gradually decrease when the internuclear distance is shortened down to R =2 Å. At R =1.4 Å, they rapidly interchange their character, in consistency with the sharp avoided crossings of states $2^3\Pi$ and $3^3\Pi$. As a consequence, the transition $1^3\Sigma^- - 2^3\Pi$ has a spike at R =1.5 Å, simultaneous to the sign change of dipole moment $1^3\Sigma^- - 2^3\Pi$, while the asymptotically forbidden $1^3\Sigma^- - 1^3\Pi$ transition dipole undergoes a sharp raise below R =1.4 Å. In summary, when decreasing the internuclear distance below R =1.8 Å, the strength of the dipole towards $2^3\Pi$ (about 0.6 ea_0) commutes successively to $3^3\Pi$ and $1^3\Pi$. Finally, the transition dipole moment between $1^3\Pi$ and $1^3\Sigma^+$ is almost constant, in concordance with the fact that both the initial and final states keep their very repulsive nature and behaviour down to R =1.2 Å without noticeable perturbation. At even shorter distance, state $1^3\Sigma^+$ interacts with $2^3\Sigma^+$, located at higher energies not visible on Fig. 2 and it is no longer present in the calculated MRCI roots.

The singlet–singlet transitions moments do not evolve strongly between $R = \infty$ and 2.8 Å. Five transitions from molecular states

Downloaded from https://academic.oup.com/mnras/article/529/3/2527/7630239 by guest on 05 May 2024

correlated with the ^{1}D asymptote to states correlated with ^{1}P^o are allowed, namely $1^1\Delta - 2^1\Pi$, $1^1\Pi - 2^1\Pi$, $1^1\Pi - 3^1\Sigma^+$, $1^1\Sigma^+ - 2^1\Pi$, and $1^1\Sigma^+ - 3^1\Sigma^+$. Their asymptotic (absolute) values are 0.34, 0.6, 0.6, 0.6, and 0.68 a_0^3, respectively, which is in line with a simple configurational description of the states, yielding transitions with ratios equal to $1/\sqrt{3}$, 1, 1, 1, and $2/\sqrt{3}$, respectively (see Appendix A1).The calculated total asymptotic line strength is 3.58 a_0^6 to be compared wit 3.60 a_0^6 experimentally (Haris & Kramida 2017). Finally two molecular transitions, $2^1\Sigma^+ - 3^1\Pi$ and $2^1\Sigma^+ - 1^1\Sigma^+$ are related to the ^{1}S–$^1P^o$ atomic one. It is shown in Appendix A1 that their asymptotic magnitudes should compare with the former at 1 with a ratio of $\sqrt{2/3}$, yielding a dipole around 0.48, which is the value observed in Fig. 4. At shorter range, the latter transition moments decrease. The $2^1\Sigma^+ - 3^1\Pi$ transition undergoes variations likely linked to the inflexion in state $2^1\Pi$ commented above. The total line strength factor is calculated to be 0.69 a_0^6 versus 0.63 a_0^6 experimentally (Haris & Kramida 2017). The transition dipoles in this work show good asymptotic consistency and are noticeably different from those of Cargnoni (2023), even at medium and long internuclear distance. Let us stress here for the present purpose of investigating atomic line broadening, the importance of the consistency of the calculated long range magnitudes of the dipole transitions with the atomic spectral data.

3 GENERAL EXPRESSION FOR THE SPECTRUM IN AN ADIABATIC REPRESENTATION

We are concerned with the pressure broadening by neutral perturbers of an isolated spectral line at perturber densities extending well above the binary collision impact approximation. In Allard et al. (1999), we derived a general expression of the autocorrelation function of Anderson & Talman (1956) to take into account the variation of the electric dipole moment during a collision. The theoretical approach is based on the quantum theory of spectral line shapes of Baranger (1958a, b) developed in an adiabatic representation to include the degeneracy of atomic levels (Royer 1974, 1980).

For isolated lines, the normalized profile $I(\Delta\omega)$ can be written as the Fourier transform (FT) of the dipole autocorrelation function $\Phi(s)$,

$$I(\Delta\omega) = \frac{1}{\pi}\, Re \int_0^{+\infty} \Phi(s) e^{-i\Delta\omega s} \mathrm{d}s \ , \tag{1}$$

where $\Delta\omega$ is the angular frequency difference from the unperturbed centre of the spectral line. $I(\Delta\omega)$ is the normalized line profile proportional to the absorption coefficient as described by Allard et al. (1999). We obtain for a perturber density n_p

$$\Phi(s) = e^{-n_p g(s)}, \tag{2}$$

where decay of the autocorrelation function with time leads to atomic line broadening. It depends on the density of perturbing atoms n_p and on their interaction with the radiating atom.

The relationship between the cross-section σ associated to each line and the normalized absorption coefficient given in equation (1) is

$$I(\Delta\omega) = \sigma(\Delta\omega)/\pi r_0 f \ , \tag{3}$$

where r_0 is the classical radius of the electron, and f is the oscillator strength of the transition.

The dipole autocorrelation function $\Phi(s)$ is evaluated for a classical collision path with an average over all possible collisions.

For a transition $\alpha = (i, f)$ from an initial state i to a final state f, we have

$$g_\alpha(s) = \frac{1}{\sum_{e,e'}{}^{(\alpha)} |d_{ee'}|^2} \sum_{e,e'}{}^{(\alpha)} \int_0^{+\infty} 2\pi\rho d\rho \int_{-\infty}^{+\infty} \mathrm{d}x \tilde{d}_{ee'}[R(0)] \left[e^{\frac{i}{\hbar}\int_0^s dt\ V_{e'e}[R(t)]} \tilde{d}^*_{ee'}[R(s)] - \tilde{d}_{ee'}[R(0)] \right]. \tag{4}$$

In equation (4), the sum $\sum_{e,e'}^{(\alpha)}$ is over all pairs (e, e') such that $\omega_{e',e}(R) \to \omega_\alpha$ as $R \to \infty$. The states of interest in this study are those which correlate with ^{1}D–^{1}P and ^{1}S–^{1}P for the singlet and ^{3}P–^{3}P^o for the triplet lines. Tables A1–A3 in Appendix A list all the involved electronic states. We also report the weights of the allowed dipole transitions and the square of the asymptotic values of their dipole moments shown in Fig. 4.

The line shapes depend on atomic interaction energy described in the previous section. We define the potential energy $V(R)$ for a state e as:

$$V_e(R) = E_e(R) - E_e^\infty, \tag{5}$$

In the present context, the perturbation of the frequency of the atomic transition during the collision results in a phase shift, $\eta(s)$, calculated along a classical path $R(t)$ that is assumed to be rectilinear. The phase shift is given by

$$\eta(s) = \frac{1}{\hbar}\int_0^s \mathrm{d}t\ V_{e'e}[R(t)], \tag{6}$$

where $\Delta V(R)$, the potential difference, is given by:

$$\Delta V(R) \equiv V_{e'e}[R(t)] = V_{e'}[R(t)] - V_e[R(t)], \tag{7}$$

and represents the difference between the electronic energies of the quasi-molecular transition.

At time t from the point of closest approach

$$R(t) = \left[\rho^2 + (x + \bar{v}t)^2\right]^{1/2}, \tag{8}$$

with ρ the impact parameter of the perturber trajectory, $\bar{v}$ is the relative velocity, and x the position of the perturber along its trajectory at time $t = 0$.

An important factor is the variation of the dipole moment during the collision once modulated by the Boltzmann factor $e^{-\beta V_e(r)}$ (equation 117 of Allard et al. 1999),

$$D(R) \equiv \tilde{d}_{ee'}[R(t)] = d_{ee'}[R(t)] e^{-\frac{\beta}{2}V_e[R(t)]}, \tag{9}$$

where β is the inverse temperature ($1/kT$). The Boltzmann factor $e^{-\frac{V_e(R)}{2kT}}$ in equation (9) appears because the perturbing atoms are in thermal equilibrium with the radiating atom, which affects the probability of finding them initially at a given R.

4 ANALYSIS OF THE COLLISIONAL PROFILES OF THE C LINES PERTURBED BY HE ATOMS

4.1 Study of the potential differences

In radiative collision transitions it is the potential difference between the final and initial states that determines the frequency and the energy emitted or absorbed by a single photon. The line wing, generally, does not decrease monotonically with increasing frequency separation from the line centre. Its shape, for an atom in the presence of other atoms is sensitive to the difference between the initial and final state interaction potentials (equation 7). When this difference

Downloaded from https://academic.oup.com/mnras/article/529/3/2527/7630239 by guest on 05 May 2024

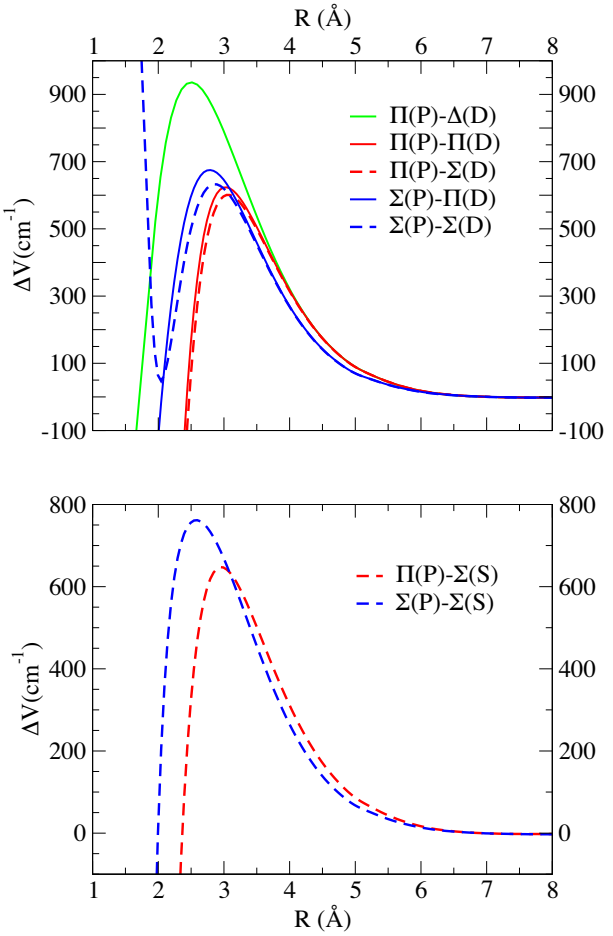

Figure 5. $\Delta V(R)$ for the transitions involved in the 1930 and 2478 Å lines. Top: potential energy differences for the five transitions contributing to the ^{1}D $\rightarrow$ ^{1}P at 1930 Å. Bottom: potential energy differences for the two transitions contributing to the ^{1}S $\rightarrow$ ^{1}P line at 2478 Å.

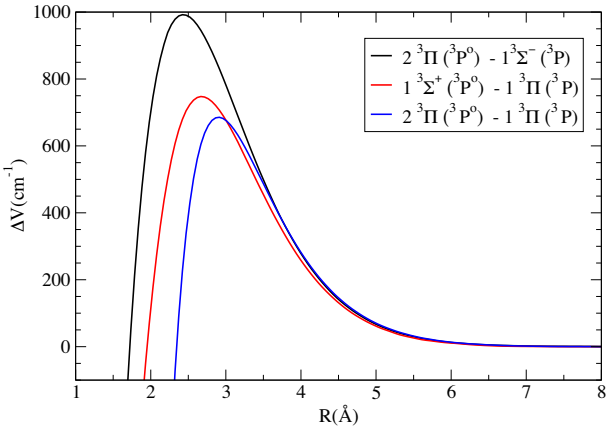

Figure 6. Potential energy differences for the three transitions contributing to the ^{3}P $\rightarrow$ ^{3}P^o line at 1657 Å.

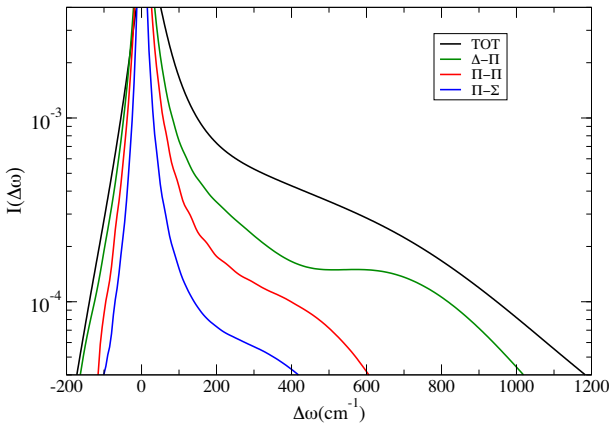

Figure 7. Individual components of the 1930 line compared to the total profile. (T $= 8000$ K and $n_{\rm He} = 10^{21}$ cm^{-3}).

$\Delta V(R)$, for a given transition, goes through an extremum, a relatively wider range of interatomic distances contribute to the same spectral frequency, resulting in an enhancement, or satellite, in the line wing (Anderson 1952; Allard 1978; Royer 1978). The difference $\Delta V(R)$ between the electronic energies of all the quasi-molecular $e'-e$ transitions are plotted in Figs 5 and 6. They all present a maximum at relatively short internuclear distance, $R_{\rm ext} = 2.5$–3 Å. Almost all $\Delta V(R)$ become negative at short internuclear distance. The only exception (top pannel of Fig. 5) is observed in the case of the singlet Σ(P)–Σ(D) potential difference which has a maximum at $R = 2.8$ Å, a minimum at $R = 2$ Å and is repulsive at very short distance. This is caused by the very steep repulsive potential slope of the upper state $3^1\Sigma^+$ and the inflexion observed in the lower state $1^1\Sigma^+$ for $R \leq 2.5$ Å, significantly reducing its repulsion in the inner region (see Fig. 3). Also note that, as a result of the sharply avoided crossing between states $2^3\Pi$ and $3^3\Pi$, the potential differences exchange their inner negative slopes at $R = 1.3$ Å (not shown in Fig. 6), without inducing new extrema at that distance. This is a case of sharply avoided crossing where the adiabatic approximation breaks down but fortunately without inducing significant contribution in the present results. The position of a line satellite depends on the value of $\Delta V(R_{\rm ext})$ but is always closer to the line centre than this value. Tables A1–A3 summarize the potential difference maxima $\Delta V(R_{\rm ext})$ and $R_{\rm ext}$ for all the allowed dipole transitions contributing to the ^{1}D $\rightarrow$ ^{1}P, ^{1}S $\rightarrow$ ^{1}P, and ^{3}P $\rightarrow$ ^{3}P^o transitions.

Fig. 7 shows the individual components of the 1930 line, weighted as if they were the only contribution to the profile. We have restricted the study to 3 transitions to make the figure clearer. The distinct wide shoulder at about 700 cm^{-1} due to $^1\Delta(^1{\rm D}) \rightarrow {}^1\Pi(^1{\rm P})$ leads to the largest extension in the blue wing. This extension is largely dependent on the accuracy of the potential difference of the contributing states to the transition, while the strength of the absorption as a function of wavelength is dependent on the radiative dipole moment shown in Fig. 8. Such analysis was restricted to the 1930 line but would lead to the same conclusion for the other lines. A general unified theory is then essential as the blue C–He quasi-molecular line satellites are blended in the near wing of the line profiles and are responsible of their asymmetry.

Blue line satellites on He lines due to He–He collisions reported in Allard et al. (2013) are due to a similar behaviour of the *ab initio* potential energies of He_2 for the $1s$–$2p$ and $2p$–$3s$ transitions which lead to maxima in all the potential energy difference. The corresponding profiles are then totally asymmetric as these C lines. Next section we will study the temperature and density dependence of the absorption cross-sections of the three lines and we will show their similar shape (Fig. 9).

Downloaded from https://academic.oup.com/mnras/article/529/3/2527/7630239 by guest on 05 May 2024

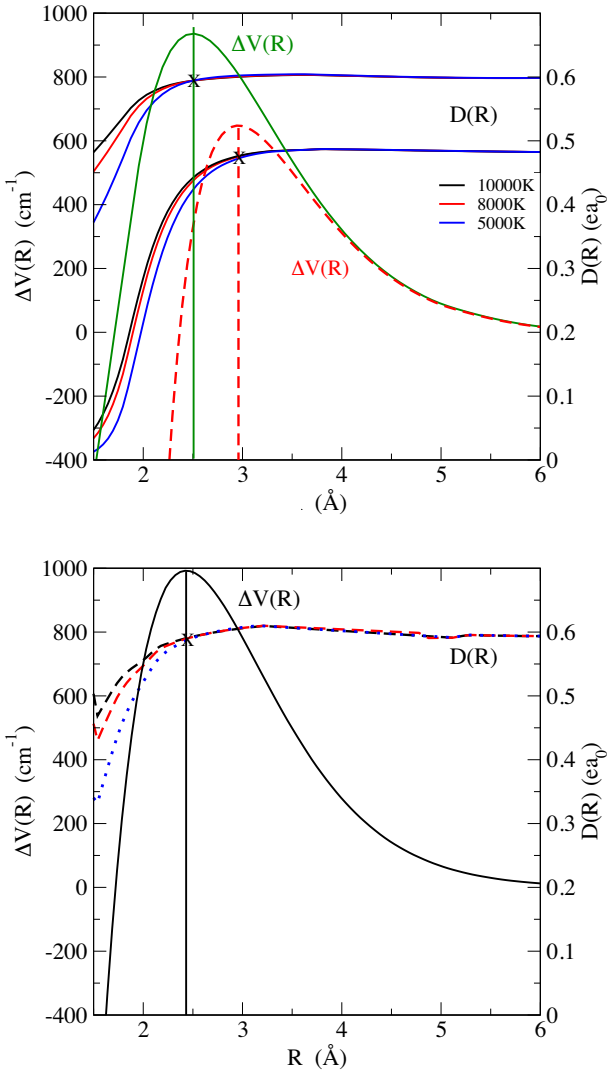

Figure 8. Top: variation with temperature in the modulated dipole [T = 10000 K (black line), T = 8000 K (red line), and T = 5000 K (dotted blue line)] and the potential difference. Π(P)–Δ(D) (green curve) and Π(P)–Σ(S) (dashed red curve) for the transitions involved in the singlet lines. Bottom: $2\,^3\Pi(^3P^o)$-$1\,^3\Sigma^-(^3P)$ for the transition involved in the 1657 triplet line.

4.2 Temperature dependence of the blue line wing

The satellite amplitude and its existence depends on the value of the electric dipole transition moment through the region of the potential difference extremum responsible of the satellite and on the position of this extremum (Allard et al. 1998, 2019, 2023; Allard, Spiegelman & Kielkopf 2007, 2016a). In Fig. 8, we show $D(R)$ together with the corresponding $\Delta V(R)$. For each line, we restrict the analysis to the transition which has either the largest maximum of $\Delta V(R)$ or the greatest weight. As we consider absorption profiles, V_e in equation (9) is $^1\Delta(^1D)$ for the transition $^1\Delta(^1D) \rightarrow {}^1\Pi(^1P)$, $^1\Sigma^+(^1S)$ for $^1\Sigma^+(^1S) \rightarrow {}^1\Pi(^1P)$ and $1\,^3\Sigma^-(^3P)$ for the transition $1\,^3\Sigma^-(^3P) \rightarrow 2\,^3\Pi(^3P^o)$. $D(R)$ is not dependent on temperature throughout the region where the line satellites are formed (Fig. 8) $D(R)$ has reached its asymptotic value in this range of temperature. As shown in Fig. 9, the blue wings of the C lines do not change with increasing temperature in the range of temperatures 5000–10 000 K and above.

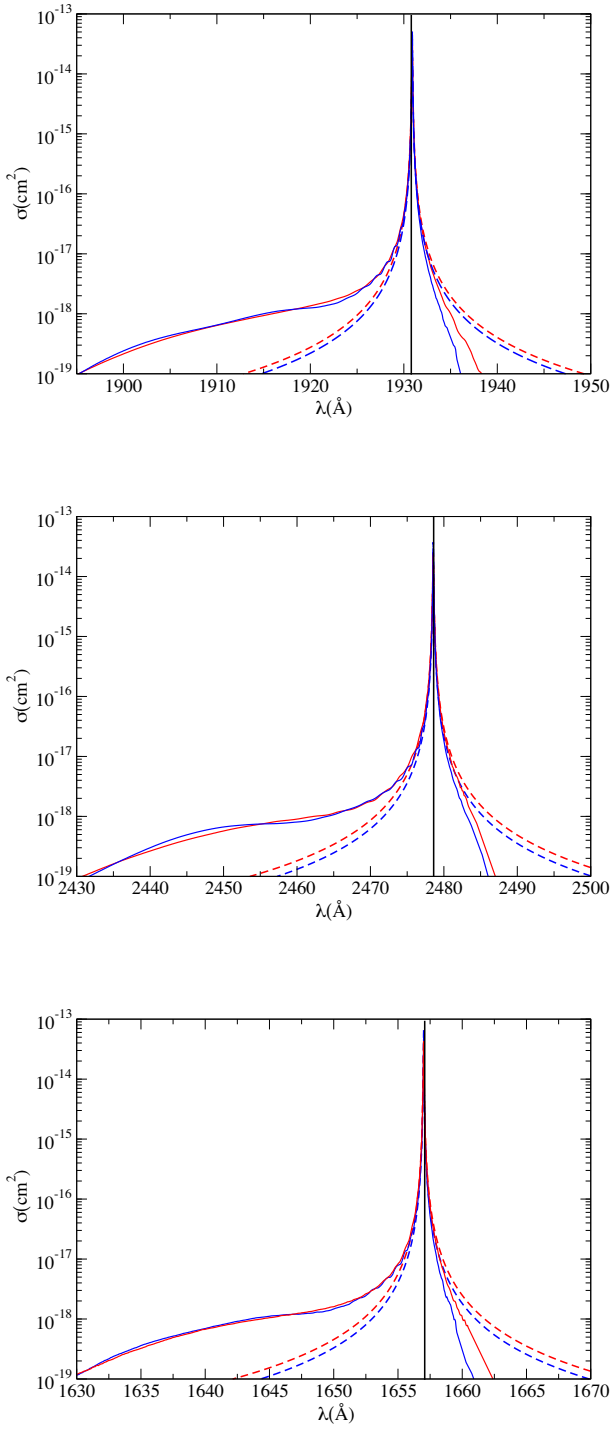

Figure 9. Temperature dependence of C 1930 (top), C 2478 (middle), and C 1657 (bottom) lines perturbed by He collisions. T = 10 000 K (red lines) and T = 5000K (blue lines). n_{He} = 2×10^{19} cm^{-3}. Lorentzian lines are reported in dashed lines. A vertical dark line shows the position of the unperturbed lines.

4.3 Line core parameters

An atomic line broadened by collisions in a low-density gas has a Lorentzian profile near the line centre which can be related to the FT of a radiative wave in which short duration collisions produce sudden phase changes. In the theory of impact broadened line shape

Downloaded from https://academic.oup.com/mnras/article/529/3/2527/7630239 by guest on 05 May 2024

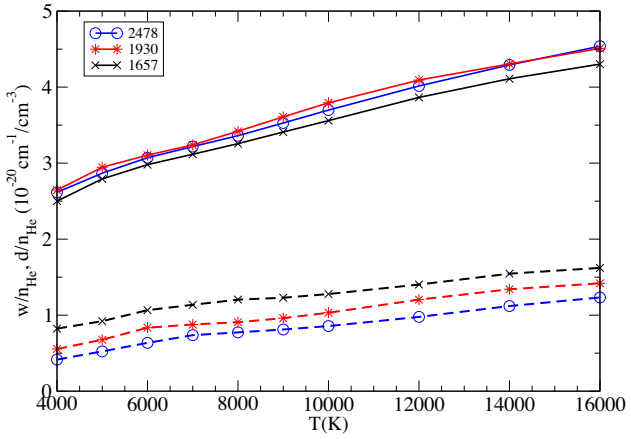

Figure 10. Variation with temperature of the broadening rate ($w/n_{\rm He}$) and shift rate ($d/n_{\rm He}$) of the C lines perturbed by He collisions. 1930 (red line), 2478 (blue line), and 1657 (black line). Line shift rates are reported in dashed lines.

the phase shifts are given by equation (6) with the integral taken between s $= 0$ and ∞.

The symmetric centre of a Lorentzian can be defined by two line parameters, the width and the shift of the main line. These quantities can be obtained in the impact limit (s $\rightarrow \infty$) of the general calculation of the autocorrelation function (equation 4). One outcome of our unified approach is that we may evaluate the difference between the impact limit and the general unified profile, and establish with certainty the region of validity of an assumed Lorentzian profile. When the helium density is less than 10^{20} cm^{-3}, the impact approximation can be used to determine the core of the line. The line width w is measured by half the full width at half the maximum intensity, what is customarily termed HWHM. The line parameters are linearly dependent on He density. Fig. 10 shows the variation of the line width w and the line shift d with temperature for the C lines. An average over velocity was done numerically by performing the calculation for different velocities and then thermally averaging with 24-point Gauss–Laguerre integration. The values of the line parameters are reported in Appendix A2 (Tables A4 and A5).

4.4 Density dependence

Several theoretical computed profiles are used to illustrate the evolution of the line satellites with pressure. The problems due to close collision effects in line profiles have been largely overviewed in our recent papers considering the Lyman and Balmer lines perturbed by helium (Spiegelman, Allard & Kielkopf 2021, 2022; Allard et al. 2022). When the perturber density gets very high the physical situation becomes quite similar to the emission spectrum in dense fluid helium excited by corona discharges at 7067 Å. The experimal spectra show an asymmetric atomic line due to the existence of near blue satellites (Allard et al. 2009). The traditional separation of line profiles into a core region to be treated by the impact approximation and a wing region to be treated by the quasi-static approximation fails to be satisfactory when very close line satellites lead to an asymmetrical shape of the line.

Top of Figs 11–13 show the development of the blue wing when the He density is increased from 2×10^{21} to 5×10^{21} cm^{-3}. There is a dramatic change when the density gets larger than 2×10^{21} cm^{-3}. The centre of the main line is overwhelmed by the line

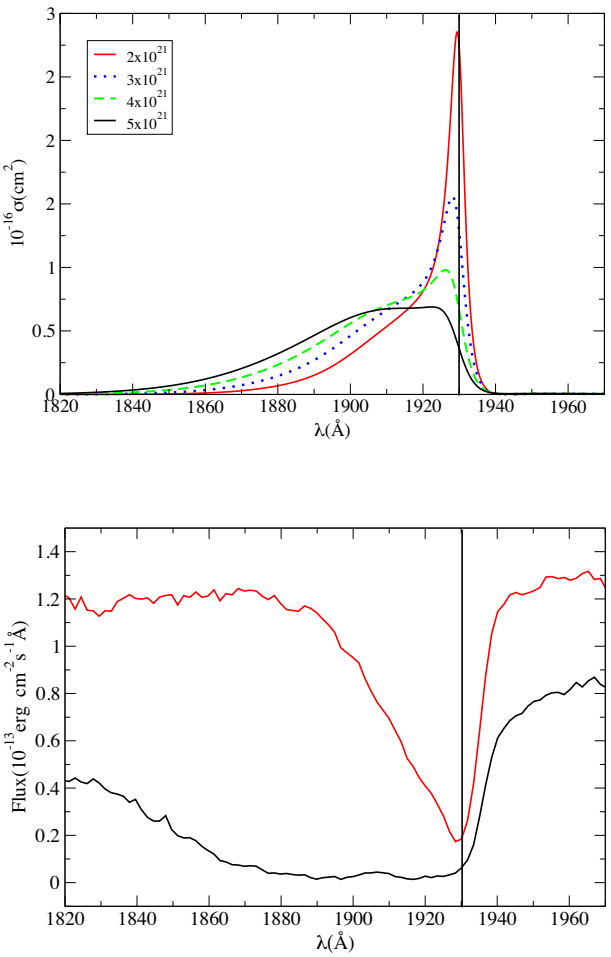

Figure 11. Top: density dependence of the 1930 line profile for He density varying from 2 to 5 $\times$ 10^{21} cm^{-3}. Bottom: *IUE* spectrum of L145-141 (Weidemann et al. 1980, black curve) and LDS687A (Oswalt et al. 1991, red curve).

satellites, increasing the He density to 5×10^{21} cm^{-3} results in a shift of the whole profile towards the position of the satellite bands.

This He density dependence explains the asymmetrical shape and shift of the observed spectra of the DQ white dwarfs in the UV. *IUE* observations of the DQ stars have been important in establishing both the effective temperatures and the C/He abundance in the photospheres in the DQ white dwarfs. A high-resolution UV spectrum of the helium-rich degenerate LDS 678A, obtained with *IUE* by Oswalt et al. (1991), is presented in Fig. 1 and in the bottom of Figs 11 and 12. They show the asymmetric profiles of the 1930 and 2478 lines. We have reported in the bottom of Fig. 11, the *IUE* spectrum of L145-141 obtained by Weidemann, Koester & Vauclair (1980). It was the first object to show a a very broadened line in the blue wing. An archive of the UV low-dispersion spectra has been achieved by Holberg et al. (2003).[1] G33-49 observed by Vauclair, Weidemann & Koester (1981, see fig. 10 of Holberg et al. 2003) also shows a very large line centred at 1910 Å with a full width at half the maximum (FWHM) $=$ 70 Å in agreement with the theoretical line profile calculation when $n_{He} = 5 \times 10^{21}$ cm^{-3} (top

[1] http://vega.lpl.arizona.edu/newsips/low

Downloaded from https://academic.oup.com/mnras/article/529/3/2527/7630239 by guest on 05 May 2024

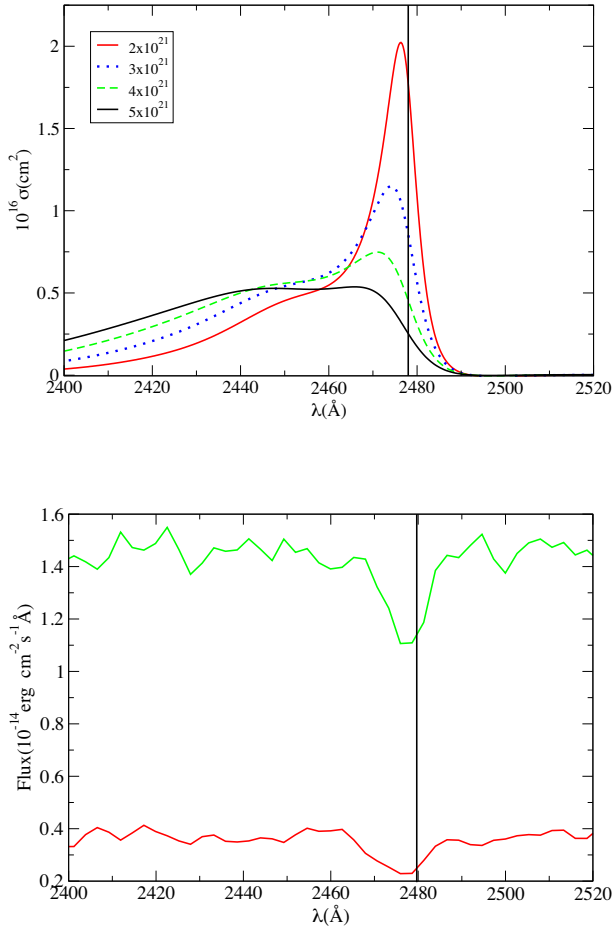

Figure 12. Top: density dependence of the 2478 line profile for He density varying from 2 to 5 × 10^{21} cm^{-3}. Bottom: *IUE* spectra of L97-3 (Koester et al. 1982, red curve) and of LDS687A (Oswalt et al. 1991, green curve).

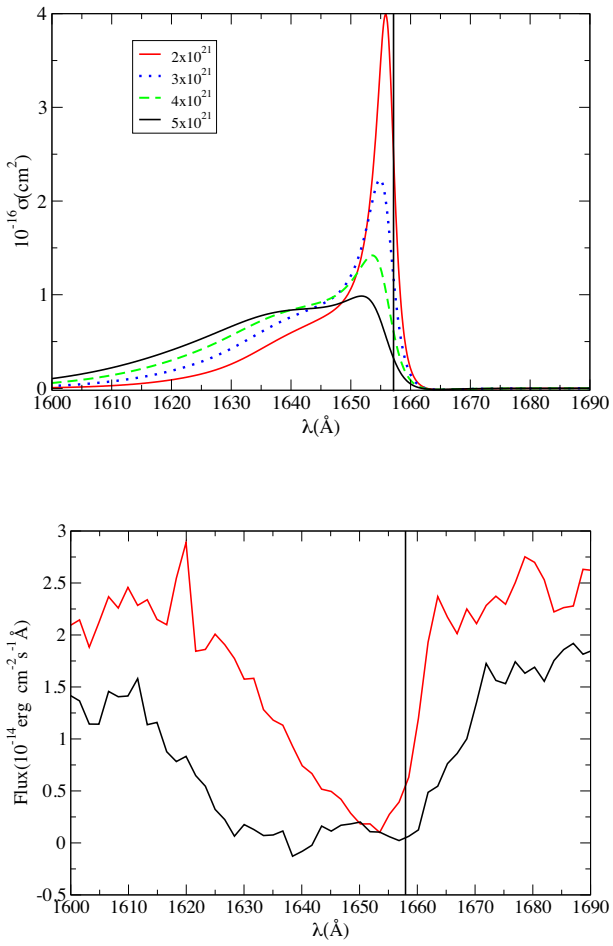

Figure 13. Top: density dependence of the 1657 line profile for He density varying from 2 to 5 × 10^{21} cm^{-3}. Bottom: *IUE* spectra of L791-40 (red curve) and L97-3 (black curve, Koester et al. 1982).

of Fig. 11). The same behaviour is reported in the bottom of Fig. 13, the very broad line centred at 1640 Å of L97-3 differs from the just asymmetrical shape of L791-40. The positions and shapes of the C lines are very dependent on the He density, the line wings are mostly formed in the lower photosphere, where high helium density should prevail in cool DQ white dwarfs, they are a test of accuracy of the models.

5 CONCLUSION

In this paper, we have determined accurate potentials and transition dipole moments for singlet–singlet and triplet–triplet transitions of CHe. We have applied a unified theory of collisional line profiles to calculate the C 1930, C 2478, and C 1657 lines of C perturbed by He collisions, including dependence upon temperature and helium density, revealing important line asymmetry strongly dependent upon helium density and consistent with several astronomical observations. One can think of possible improvements of this work. The first one would be the determination of potentials including spin–orbit (SO) coupling for triplet states. Account of SO coupling would obviously complexify the situation in several ways. SO coupling splits the atomic and molecular states and hence multiplies the number of transitions. The SO coupling constants can be estimated around 15 and 20 cm^{-1} for the ^{3}P and ^{3}P^o configurations, respectively, from the atomic data tables (Haris & Kramida 2017), that is of the similar magnitude or even larger than that of some of the medium and long distance well depths. At those distances where the SO parent states are still close to each other, account of SO coupling induces crossings or avoided crossings between the fine-structure state potentials, and hence change their characteristics, as shown by Le Picard et al. (2002) who did specifically investigate collisional non-adiabatic transitions between the ^3P fine structure atomic components. Conversely at shorter distance, the parent state potentials acquire significantly different repulsive shapes, the influence of SO coupling becomes only perturbative and is expected to be quantitatively much smaller. The main quasi-molecular satellites in this work occur around maxima in the potential differences located at distances below 3 Å. In this distance range, the repulsive potentials differ by a few tens or a few hundreds cm^{-1}, significantly larger than the SO coupling magnitude. Nevertheless, account of SO coupling would allow to get further insight (fine structure) and greater accuracy in the spectra close to the line centres. It would then be relevant to consider the non-adiabatic couplings between fine-structure adiabatic states, not included in the unified line shape scheme used here. This would be a second improvement of the present calculations, also providing a better account of closely avoided crossings even not considering SO coupling, like for instance that between the $^3\Pi$ states.

Downloaded from https://academic.oup.com/mnras/article/529/3/2527/7630239 by guest on 05 May 2024

Considering the astrophysical aspects, we have more specifically discussed the case of DQ dwarf stars. For DQ white dwarf stars in the temperature range where both atomic lines and molecular bands are present, the atmosphere models have difficulties reproducing both types of absorption features simultaneously. This inability to accurately describe the UV and optical flux in cool DQ white dwarfs is due to the inadequacy of the input physics. Inaccurate opacities result in systematic errors in the predicted flux distribution and hence in the effective temperature and chemical abundances. The abundances determined from the UV or the optical differs by a factor 30 in the case of Procyon B (Provencal et al. 2002). The observed carbon abundance in the atmosphere is directly related to the thickness of the helium layer remaining from the previous nuclear evolution, which is a very important parameter for the understanding of stellar evolution (Dufour, Bergeron & Fontaine 2005). In this paper, we have shown that collision-broadened C–He lines show features, as unresolved line satellites, for which their presence is sensitive to the conditions of the radiating system. In conclusion, complete unified line profiles, valid at high helium densities and based on accurate atomic and molecular physics should be incorporated into the analysis of cool DQ white dwarf spectra to describe correctly the asymmetrical shape of the C I lines in the UV.

ACKNOWLEDGEMENTS

We thank the referee for helpful comments that improved the manuscript.

DATA AVAILABILITY

The CHe potentials and dipole moments can be obtained upon request from F. Spiegelman and the CHe line profiles from N. F. Allard.

REFERENCES

Allard N. F., 1978, J. Phys. B: At. Mol. Opt. Phys., 11, 1383
Allard N. F., Drira I., Gerbaldi M., Kielkopf J. F., Spielfiedel A., 1998, A&A, 335, 1124
Allard N. F., Royer A., Kielkopf J. F., Feautrier N., 1999, Phys. Rev. A, 60, 1021
Allard N. F., Spiegelman F., Kielkopf J. F., 2007, A&A, 465, 1085
Allard N. F., Deguilhem B., Gadéa F. X., Bonifaci N., Denat A., 2009, Europhys. Lett., 88, 53002
Allard N. F., Deguilhem B., Monari A., Gadéa F. X., Kielkopf J. F., 2013, A&A, 559, A70
Allard N. F., Spiegelman F., Kielkopf J. F., 2016a, A&A, 589, A21
Allard N. F., Guillon G., Alekseev V. A., Kielkopf J. F., 2016b, A&A, 593, A13
Allard N. F., Spiegelman F., Leininger T., Molliere P., 2019, A&A, 628, A120
Allard N. F., Spiegelman F., Kielkopf J. F., Bourdreux S., 2022, A&A, 657, A121
Allard N. F., Myneni K., Blakely J. N., Guillon G., 2023, A&A, 674, A171
Anderson P. W., 1952, Phys. Rev., 86, 809
Anderson P. W., Talman J. D., 1956, Technical Report 3117. Bell System, Murray Hill NJ
Baranger M., 1958a, Phys. Rev., 111, 481
Baranger M., 1958b, Phys. Rev., 111, 494
Bergeat A., Chefdeville S., Costes M., Morales S. B., Naulin C., Even U., Kłos J., Lique F., 2018, Nat. Chem., 10, 519
Cargnoni F., 2023, Chem. Phys. Lett., 826, 140674
Dufour P., Bergeron P., Fontaine G., 2005, ApJ, 627, 404
Haris K., Kramida A., 2017, ApJS, 233, 16
Holberg J. B., Barstow M. A., Burleigh M. R., 2003, ApJ, 147, 145
Koester D., Weidemann V., Zeidler E. M., 1982, A&A, 116, 147
Kramida A., Ralchenko Yu., Reader J., NIST ASD Team, 2022, NIST Atomic Spectra Database (ver. 5.10). National Institute of Standards and Technology, Gaithersburg, MD, [Online]. Available at: https://physics.nist.gov/asd [2023, November 24]
Lavendy H., Robbe J.-M., . Roueff E., 1991, A&A, 241, 317
Le Picard S. D. et al., 2002, J. Chem. Phys., 117, 10109
Oswalt T. D., Sion E. M., Hammond G., Vauclair G., Liebert J. W., Wegner G., Koester D., Marcum P. M., 1991, AJ, 101, 583
Partridge H., Stallcop J. R., Levin E., 2001, J. Chem. Phys., 115, 6471
Pelletier C., Fontaine G., Wesemael F., Michaud G., Wegner G., 1986, Ap J, 307, 242
Provencal J. L., Shipman H. L., Wesemael F., Bergeron P., Bond H. E., Liebert J., Sion E. M., 1997, ApJ, 480, 777
Provencal J. L., Shipman H. L., Koester D., Wesemael F., Bergeron P., 2002, ApJ., 568, 324
Royer A., 1974, Can. J. Phys., 52, 1816
Royer A., 1978, Acta Phys. Pol. A, 54, 805
Royer A., 1980, Phys. Rev. A, 22, 1625
Schwerdtfeger P., Nagle J. K., 2019, Mol. Phys., 117, 1200
Spiegelman F., Allard N. F., Kielkopf J. F., 2021, A&A, 651, A51
Spiegelman F., Allard N. F., Kielkopf J. F., 2022, A&A, 659, A157
Staemmler V., Flower D.. R., 1991, J. Phys. B: At. Mol. Opt. Phys., 24, 2343
Szudy J., Baylis W., 1975, J. Quant. Spectrosc. Radiat. Transfer, 15, 641
Vauclair G., Weidemann V., Koester D., 1981, A&A, 100, 113
Weidemann V., Koester D., 1995, A&A, 297, 216
Weidemann V., Koester D., Vauclair G., 1980, A&A, 83, L13
Werner H. J., Knowles P. J., 1988, J. Chem. Phys., 89, 5803
Werner H.-J. et al., The Molpro quantum chemistry package, J. Chem. Phys., 2020, 152, 144107, available at: , Molpro is available at http://www.molpro.net

APPENDIX A: SUPPLEMENTARY INFORMATION

A1 Asymptotic limits of the CHe dipole transition moments

We consider here a simple description of the states as single configuration with Ccartesian orbital functions, For sake of simplicity, we omit here the always doubly occupied 1s orbital of Helium as well as the 1s and 2s orbitals of Carbon, considered as always doubly occupied and we express the atomic $2p^2$ and 2p3s states as configurations built on determinants (defined within vertical bars). In the following, α orbitals have no bar, while β spin orbitals have a bar. The application of the Slater rules for the for the components X, Y, and Z provides expressions of the monoelectronic dipolar transition operators $\mathbf{R} = \sum_i \mathbf{r}(i)$

Table A1. Allowed transitions between ^{1}D–^{1}P involved in the 1930 Å line.

Upper level	Lower level	Weight	$\Delta V(R_{ext})$ (cm^{-1})	R_{ext}(Å)	d^2
$^1\Pi(^1P)$	$^1\Delta(^1D)$	4	936	2.5	0.357
$^1\Pi(^1P)$	$^1\Pi(^1D)$	2	623	3.04	0.355
$^1\Pi(^1P)$	$^1\Sigma^+(^1D)$	2	600	3.04	0.12
$^1\Sigma^+(^1P)$	$^1\Pi(^1D)$	2	675	2.8	0.367
$^1\Sigma^+(^1P)$	$^1\Sigma^+(^1D)$	1	633	2.8	0.47

Downloaded from https://academic.oup.com/mnras/article/529/3/2527/7630239 by guest on 05 May 2024

A1.1 Molecular transitions related to ^3P–$^3P^o$

$$\begin{aligned}
\lim_{R\to\infty} < 1^3\Sigma^-_| Y|2^3\Pi_x > &= < (|2p_x 2p_y|)|eY[(|2p_x 3s|) > \\
&= < 2p_y|y|3s > \\
\lim_{R\to\infty} < 1^3\Pi_x|Z|2^3\Pi_x > &= < (|2p_x 2p_z|)|Z|'|2p_x 3s|) > \\
&= < 2p_z|z|3s > \\
\lim_{R\to\infty} < 1^3\Pi_x|X|2^3\Sigma^+ > &= < (|2p_x 2p_z|)|X|(|3s 2p_z)| > \\
&= < 2p_x|x|3s >
\end{aligned}$$

A1.2 Molecular transitions related to ^1S–^1P

$$\begin{aligned}
\lim_{R\to\infty} < 2^1\Sigma^+|X|2^1\Pi_x > &= < \frac{1}{\sqrt{3}}(|2p_x 2\bar{p}_x| + |2p_y 2\bar{p}_y| \\
&\quad +|2p_z 2\bar{p}_z)|eX|\frac{1}{\sqrt{2}}(|2p_x 3\bar{s}| \\
&\quad -|2\bar{p}_x 3s|) >= \sqrt{\frac{2}{3}} < 2p_x|x|3s > \\
\lim_{R\to\infty} < 2^1\Sigma^+|Z|3^1\Sigma^+ > &= < \frac{1}{\sqrt{3}}(|2p_x 2\bar{p}_x| + |2p_y 2\bar{p}_y| \\
&\quad +|2p_z 2\bar{p}_z)||eZ|\frac{1}{\sqrt{2}}(|2p_z 3\bar{s}| \\
&\quad -|2\bar{p}_z 3s)| >= \sqrt{\frac{2}{3}} < 2p_z|z|3s >
\end{aligned}$$

Table A2. Allowed transitions between ^{1}S–^{1}P involved in the 2478 Å line.

Upper level	Lower level	Weight	$\Delta V(R_{\rm ext})$ (cm^{-1})	$R_{\rm ext}$(Å)	d^2
$^1\Pi(^1P)$	$^1\Sigma^+(^1S)$	2	648	2.94	0.23
$^1\Sigma^+(^1P)$	$^1\Sigma^+(^1S)$	1	762	2.6	0.23

Table A3. Allowed transitions between ^{3}P–^{3}P^o involved in the 1657 Å line.

Upper level	Lower level	Weight	$\Delta V(R_{\rm ext})$ (cm^{-1})	$R_{\rm ext}$(Å)	d^2
$2\,^3\Pi(^3P^o)$	$1\,^3\Sigma^-(^3P)$	6	992	2.4	0.37
$2\,^3\Pi(^3P^o)$	$1\,^3\Pi(^3P)$	6	686	2.91	0.38
$1\,^3\Sigma^+(^3P^o)$	$1\,^3\Pi(^3P)$	6	748	2.7	0.37

A1.3 Molecular transitions related to ^1D–^1P

$$\begin{aligned}
\lim_{R\to\infty} < 1^1\Sigma^+|X|2^1\Pi_x > &= < \frac{1}{\sqrt{6}}(2|2p_z 2\bar{p}_z| - |2p_x 2\bar{p}_x| \\
&\quad -||2p_y 2\bar{p}_y|)|X|\frac{1}{\sqrt{2}}(|2p_x 3\bar{s}| \\
&\quad -|2\bar{p}_x 3s|) >= -\frac{1}{\sqrt{3}} < 2p_x|x|3s > \\
\lim_{R\to\infty} < 1^1\Delta_{xy}|Y|2^1\Pi_x > &= < \frac{1}{\sqrt{2}}(|2p_x 2\bar{p}_y| - |2p_y 2\bar{p}_y|) \\
&\quad |Y|\frac{1}{\sqrt{2}}(|2p_x 3\bar{s}| - |2\bar{p}_x 3s|) > \\
&= < 2p_y|y|3s > \\
\lim_{R\to\infty} < 1^1\Pi_x|Z|3^1\Pi_x > &= < \frac{1}{\sqrt{2}}(|2p_x 2\bar{p}_z - |2p_z 2\bar{p}_x|) \\
&\quad |Z|\frac{1}{\sqrt{2}}(|2p_x 3\bar{s}| - |2\bar{p}_x 3s|) > \\
&= < 2p_z|z|3s > \\
\lim_{R\to\infty} < 1^1\Pi_x|X|2^1\Sigma^+ > &= < \frac{1}{\sqrt{2}}(|2p_x 2\bar{p}_z - |2p_z 2\bar{p}_x|) \\
&\quad |X|\frac{1}{\sqrt{2}}(|2p_z 3\bar{s}| - |2\bar{p}_z 3s|) > \\
&= < 2p_x|x|3s > \\
\lim_{R\to\infty} < 1^1\Sigma^+|Z|3^1\Sigma^+ > &= < \frac{1}{\sqrt{6}}(2|2p_z 2\bar{p}_z - |2p_x 2\bar{p}_x| \\
&\quad -||2p_y 2\bar{p}_y|)|Z|\frac{1}{\sqrt{2}}(|2p_z 3\bar{s}| \\
&\quad -|2\bar{p}_z 3s|) >= \frac{2}{\sqrt{3}} < 2p_z|z|3s >
\end{aligned}$$

One must then consider molecular state spatial degeneracies and the following equivalences, whatever the spin symmetry

$$\begin{aligned}
< \Sigma^+|X|\Pi_x > &= < \Sigma^+|Y|\Pi_y > \\
< \Sigma^-|X|\Pi_x > &= < \Sigma^-|Y|\Pi_y > \\
< \Pi_x|Z|\Pi_x > &= < \Pi_y|Z|\Pi_y > \\
< \Delta_{xy}|Y|\Pi_x > &= < \Delta_{xy}|X|\Pi_y > \\
&= < \Delta_{x^2-y^2}|X|\Pi_x > \\
&= - < \Delta_{x^2-y^2}|Y|\Pi_y >
\end{aligned}$$

which contribute to the weights of the components together with the spin degeneracy factors.

Downloaded from https://academic.oup.com/mnras/article/529/3/2527/7630239 by guest on 05 May 2024

A2 Line parameters

Table A4. Theoretical broadening rates w/n_{He} (10^{-20} cm^{-1}/cm^{-3}) of the C lines perturbed by He collisions.

Line	4000 K	5000 K	6000 K	7000 K	8000 K	9000 K	10 000 K	12 000 K	14 000 K	16 000 K
1930	2.65	2.95	3.1	3.24	3.4	3.6	3.8	4.1	4.31	4.51
2478	2.62	2.87	3.1	3.2	3.4	3.5	3.7	4.	4.3	4.54
1657	2.5	2.8	3.	3.1	3.26	3.4	3.56	3.86	4.1	4.3

Table A5. Line shift rates (d/n_{He} (10^{-20} cm^{-1}/cm^{-3}) of the C lines perturbed by He collisions.

Line	4000 K	5000 K	6000 K	7000 K	8000 K	9000 K	10 000 K	12 000 K	14 000 K	16 000 K
1930	0.56	0.68	0.84	0.88	0.91	0.96	1.03	1.2	1.3	1.4
2478	0.42	0.52	0.64	0.74	0.77	0.81	0.86	0.98	1.1	1.2
1657	0.82	0.92	1.1	1.14	1.2	1.23	1.3	1.4	1.5	1.6

This paper has been typeset from a TEX/LATEX file prepared by the author.

Downloaded from https://academic.oup.com/mnras/article/529/3/2527/7630239 by guest on 05 May 2024

© 2024 The Author(s).
Published by Oxford University Press on behalf of Royal Astronomical Society. This is an Open Access article distributed under the terms of the Creative Commons Attribution License (http://creativecommons.org/licenses/by/4.0/), which permits unrestricted reuse, distribution, and reproduction in any medium, provided the original work is properly cited.